Environmental Science Nano

Comparative study of the elemental composition of metal(loid)-bearing nanomaterials in wildland-urban interface fire ashes using icp-TOF-MS

Journal:	*Environmental Science: Nano*
Manuscript ID	EN-ART-12-2024-001142.R1
Article Type:	Paper

Environmental Implication

This study demonstrated the abundance and elemental makeup of metal(loid) incidental nanomaterials (INMs) in wildland-urban interface (WUI) fire ashes. The identified INMs include single metal INMs such as Al, Ba, Cr, Cu, Ti, Pb, and Zn, as well as multi-metal(loid) INMs such as $CuCrO_2$, $CuCr_2O_4$, $CrAsO_4$ and SnSbPb alloys. The identification of these INM phases and transformations have important implications for the impacts of WUI fires on the biogeochemical cycling of metals and environmental and human health.

Comparative study of the elemental composition of metal(loid)-bearing nanomaterials in wildland-urban interface fire ashes using icp-TOF-MS

Mahbub Alam[1*], Sheryl A. Singerling[2], Mahdi Erfani[3], Charles N. Alpers[4], Mohammed Baalousha[1*]

[1] Center for Environmental Nanoscience and Risk, Department of Environmental Health Sciences, Arnold School of Public Health, University of South Carolina, Columbia, SC, 29208, U.S.A

[2] National Center for Earth and Environmental Nanotechnology Infrastructure (NanoEarth), Institute for Critical Technology and Applied Science, Virginia Polytechnic Institute and State University, Blacksburg, VA, 24061, U.S.A

[3] Department of Civil and Environmental Engineering, University of South Carolina, SC 29208, U.S.A

[4] U.S. Geological Survey, California Water Science Center, 6000 J Street, Sacramento, CA 95819, U.S.A

*** Corresponding Author**

Center for Environmental Nanoscience and Risk, Department of Environmental Health Sciences, Arnold School of Public Health, University of South Carolina, Columbia, SC, 29208, U.S.A

Email: mbaalous@mailbox.sc.edu

Abstract

This study investigates the abundance and elemental composition of metal(loid) incidental nanomaterials (INMs) in wildland-urban interface (WUI) fire ashes from different sources, including vegetation, structures, and vehicles, collected following the 2020 LNU (the Sonoma-Lake-Napa unit) Lightning Complex Fire in California. Particle number concentrations, elemental compositions and ratios, and size distributions were determined by single particle inductively coupled plasma-time of flight-mass spectrometry (SP-ICP-TOF-MS) coupled with automated two-stage hierarchical clustering analysis. Iron- and Mn-bearing INMs accounted for >80% of INMs detected in vegetation and atmospheric deposition ashes but they represented <50% of all INMs in structural and vehicle ashes. Together, Al, Ba, Cr, Cu, Ti, Pb, and Zn-bearing INMs accounted for 45 to 75% of all INMs in structural and vehicle ashes and 7 to 13% in vegetation and atmospheric deposition ashes. The sizes of INMs varied between a few tens to a few hundreds of nanometers with larger Ba, Cr, Fe, Ti, Pb, and Zn-bearing INMs in structural and vehicles ashes than in vegetation ashes. Several types of multi-element INMs were identified by SP-ICP-TOF-MS including chromated-copper-arsenate-related NMs (*e.g.,* $CuCrO_2$, $CuCr_2O_4$, $CrAsO_4$); CuSn and CuPb alloys; SnPb, SbPb, and SnSb alloys; and CoAl alloys. Overall, this study demonstrates the abundance and elemental makeup of various metal(loid) INMs in WUI fire ashes. This study highlights t research opportunities into the discovery, transformation, reactivity, fate, and effects of INMs during and following WUI fires.

1. Introduction

Wildland-urban interface (WUI) fires are currently receiving global attention due to increases in fire frequency, size, and severity.[1, 2] In addition, the spread of fires into the built environment results in increased emissions of different classes of contaminants of emerging concern,[3, 4] many of which remain unknown and have the potential to threaten environmental and human health. In recent years, wildfires have become increasingly destructive in the western United States due to rising temperatures from climate change, a prevalence of fuels due to long-term fire suppression, and an increased population living in proximity to wildland vegetation.[5-8] For instance, the area burned by wildfires across the United States increased from 1.3 million acres in 1983 to 7.1 million acres in 2021, with the 2020 fire season consuming a record 10.1 million acres of wildland.[9] Additionally, the number of structures burned in WUI fires has increased from around 5,200 structures, including 3,500 houses in 2011, to 18,000 structures, including 9,600 houses in 2020 (approximate increases of 246% for structures and 174% for houses burned in 10 years).[5, 9]

Fire activity at the WUI and the associated contaminant release and environmental and human health impacts are projected to increase globally due to climate and societal changes, increasing the need to improve understanding of the impacts of wildfires.[10, 11] For instance, several studies have demonstrated the release of various classes of contaminants as a result of WUI fires, including pyrogenic carbon, polycyclic aromatic hydrocarbons, polychlorinated dioxins and furans, volatile organic compounds, metals, metalloids, environmentally persistent free radicals, nutrients, and other contaminants.[12-16] However, to date, information on the formation, release, concentrations, and properties of metal(loid) incidental nanomaterials (INMs, unintentionally formed materials resulting from direct or indirect human influence consisting of solid particles where at least 50% of these particles in the number size distribution are in the size range of 1 to 100 nm[17]) as a result of WUI fire remain scarce.[18-20]

The nature and concentration of metal(loid)s in wildfire ash have been well studied [21-25]. However, less is known about the nature and concentrations of metal(loid)s in WUI fire ash which are heavily influenced by anthropogenic materials used in the urban environment. A few studies investigated metal

concentrations in WUI fire ashes[18-20, 26], soils impacted by WUI fires[18, 27, 28], and streams following WUI fires[29]. These studies demonstrated higher levels of metal(loid)s in structural and vehicle ash compared to vegetation ash[18, 26, 30, 31], higher concentration of metal(loid)s in structural ash compared to uncontaminated soils [27], and higher levels of some metals (*e.g.,* Zn, Cu, Cr, and Pb) in soils in burned residential properties compared to those in soils in non-burned residential properties and compared to those in burned non-residential (grassland) areas[28]. Metals in WUI fire ash has also been shown to contribute to up to 200-fold increase in metal concentrations in streams receiving runoff from burned areas compared to streams receiving runoff from unbummed areas [29]. These studies focused on quantifying metal concentrations in WUI fire ash, soils, and streams impacted by WUI fires and did not investigate the form in which metal(loid)s occur in these environmental media. Our recent studies of WUI fire ashes demonstrated that metal(loid)s occurs dominantly in the form of INMs in ashes, including Ti, Fe, Zn, Cr, As-oxides, $CuCr_2O_4$, $CuCrO_2$, $CrAsO_4$, $Cr_2As_4O_{12}$, and CrCuAs.[18-20] The Ti, Fe, Zn, and Cr-particles were identified by transmission electron microscopy coupled with energy dispersive X-ray spectroscopy (TEM-EDS)[18] in samples enriched with these elements. Other INMs could be present in WUI fire ash at much lower frequency than the dominant/major INM s, making impossible to identify such particles by TEM-EDS. Additionally, pragmatically, a few particles are typically measured by TEM-EDS due to time and cost limitations. Chromium, As, $CuCr_2O_4$, $CuCrO_2$, $CrAsO_4$, $Cr_2As_4O_{12}$, and CrCuAs phases were identified using (single particle)-inductively coupled plasma-time of flight-mass spectroscopy ((SP)-ICP-TOF-MS) in three green WUI fire ashes which were suspected to originate from chromated copper arsenate treated wood[19].

This study aims to investigate the concentrations, elemental makeup, and size distribution of INMs at the single particle level in WUI fire ashes derived from different fuel sources, including vegetation, structure, vehicle, and atmospheric deposition using SP-ICP-TOF-MS. We hypothesize that nanomaterials in WUI fire ashes derived from different fuel sources display distinct elemental composition and fingerprints with structural and vehicle ashes being more enriched in anthropogenic INM compared to vegetation ashes. To this end, nine ash samples —including two vegetation, one atmospheric

deposition, three structural, and three vehicle or mixed vehicle/structural ashes— were selected as representative of members of ash generated at the WUI fires. The bulk elemental composition of the ashes was determined using ICP-TOF-MS following microwave-assisted acid digestion. The multi-element single particle compositions and size distributions of INMs were determined by SP-ICP-TOF-MS with the aim to demonstrate the method capability to identify minor INM phases that cannot be determined by TEM-EDS due to their low frequency relative to the more dominant phases such as Al, Fe, and Ti. SP-ICP-TOF-MS measures the multi-elemental composition of thousands of particles within a short period of time overcoming the statistical limitations posed by the few number of particles that can be pragmatically analyzed by TE-EDS. .

2. Materials and Methods

2.1. Study Site

Ash samples were collected from burned vegetations, structures, and vehicles within the area of the LNU Lightning Complex Fire (Sonoma-Lake-Napa unit) in California during October 7-16, 2020 (**Table S1, Figures S1**).[18, 20] This fire burned 1,470 km^2 and destroyed 1,491 structures in Colusa, Lake, Napa, Sonoma, Solano, and Yolo Counties, approximately 60 km west of Sacramento, between August 17 and October 2, 2020 (**Figure S1**). Within the fire perimeter, the distribution of burn severity was 12% low, 39% moderate, and 49% high [20]. Land use in the fire perimeter consisted of 57% shrub/scrub, 19% herbaceous, 12% evergreen forest, and 1.4% developed. Two ash samples (A1 and A2) were collected from burned vegetation in forested areas far away from any human-made structures minimizing the potential contribution of structural and vehicle ashes to the vegetation ashes. Three ash samples were collected from specific locations within burned residential structures (A4, A5, and A6) and three ash samples were collected from near or underneath burned vehicles or vehicle / tool storage areas (A7, A8, and A9, **Table S1**), minimizing the potential contribution of vegetation ashes to the collected structural and vehicle ashes. In addition, a sample of air-fall ash (A3) was collected from a car's windshield during the 2019 fire season near the North Complex Fire area.[18, 20] The primary source of the atmospheric air-fall

ash was dominantly combustion of biomass. Ash samples were collected with disposable plastic scoops and placed into zippered plastic bags. All samples were collected prior to any rain or other precipitation to avoid sample alteration and losses by the rain. All ashes were homogenized using a ceramic mortar and a ceramic pestle and sieved using a 10-mesh (2 mm pore size) nylon sieve (Zhangxing Instrument, Hangzhou, Zhejiang, China) to remove large debris. The sieved samples were stored in 250 mL acid-washed high-density polyethylene (HDPE) bottles in a –20 °C freezer before further treatment.

2.2. Metal(loid) and Nanomaterial Analysis

The bulk metal(loid) concentrations in the fire ash were determined using ICP-TOF-MS following microwave assisted acid digestion as performed elsewhere [18] and summarized in the supplementary information (SI). Nanomaterials were extracted from ash using cloud point extraction following the protocol described in the SI. The extracted nanomaterials were bath sonicated for 15 min and were diluted by a factor of 100,000 prior to SP-ICP-TOF-MS analysis to avoid coincidence and eliminate dissolved background. The elemental particle composition at the individual particle level was determined by SP-ICP-TOF-MS (TOFWERK, Thun, Switzerland).[19, 32, 33] Briefly, INM suspensions were introduced into the ICP with a 2DX autosampler (Element Scientific, Omaha, Nebraska, USA) and a MicroMist U-series Nebulizer (Thermo Scientific, Waltham, Massachusetts, USA) connected via a Quartz Cyclonic Spray Chamber (Meinhard, Golden, Colorado, USA) to the injector of the ICP torch. The instrument operating parameters and the monitored isotopes are summarized in **Tables S2 and S3**, respectively. Element specific instrument sensitivities were measured with a series of multi-element solutions prepared from a mixed multi-element ICP certified reference standard (0, 1, 2, 5, and 10 $\mu g L^{-1}$ multi-element standard, diluted in 1% HNO_3, BDH Chemicals, Radnor, Pennsylvania, USA). The transport efficiency was calculated via the known size method using a 60-nm Au nanoparticles national institute standard and technology standard reference materials (NIST SRM 8013, Gaithersburg, Maryland, USA) and a series of ionic Au standards (BDH Chemicals, West Chester, Pennsylvania, USA) [34]. A 4.5% H_2/He gas mixture was used as collision gas to eliminate/minimize interferences and was optimized for $^{56}Fe^+$ and $^{28}Si^+$ signals. All data processing, including signal thresholding (Poisson algorithm [35]) and split event

correction, was performed using Tofpilot (Version 2.9, TOFWERK, Thun, Switzerland). The sample-specific mass and size detection limits were calculated according to according to the Poisson distribution using the background signal within each sample and are summarized in **Table S3**. The mass and size detection limit of each element varied within a narrow range between the different samples due to the significant dilution (100,000 folds) of the samples. All samples and ultrapure water blanks were analyzed in triplicate, and data were acquired for 200 s for each replicate. After verifying the reproducibility of the single particle elemental composition and number concentrations among the replicates the three replicates were combined to achieve comprehensive analysis due to limited detection events of certain elements.

2.3. Clustering analysis of multi-metal(loid) nanomaterials

The detected nanomaterials (NMs) were classified into single- and multi-metal(loid) nanomaterials (smNMs and mmNMs, respectively). The mmNMs were further classified into clusters of mmNMs of similar elemental composition using two-stage (*e.g.,* intra- and inter-sample) automated agglomerative hierarchical clustering analysis performed in MATLAB as described elsewhere.[32, 33, 36] Intra-sample clustering was performed on all metal(loid) masses in each NM using average correlation distance to generate clusters that best account for variance in NM composition in each sample. The generated clusters were grouped into major clusters using an optimal distance cutoff. A cluster representative was determined for each major cluster as the mean of metal(loid) mass in individual NMs within each cluster accounting for all elements that occurred in at least 5% of NMs within the cluster. The mean intra-sample cluster composition was determined as the mean of metal(loid) mass fraction in all NMs in the cluster and was compared across samples. Inter-sample clustering was performed on the major cluster representatives identified in the intra-sample clustering to group/cluster the similar NM major clusters identified in the different samples. Major/similar clusters were identified using an optimal cutoff which was determined by maximizing the mean silhouette score for each sample. The silhouette score is a measure of how similar a NM is to its own cluster (cohesion) compared to other clusters (separation).[37] Thus, silhouette coefficient provides a measure of how well each NM has been classified.[37] The silhouette score ranges from −1 to +1, where a high value indicates that a NM is well matched to its own cluster and poorly matched to

neighboring clusters (far away from the neighboring clusters). In contrast, 0 indicates that a NM is on or very close to the decision boundary between two neighboring clusters. A negative value indicates that a NM might have been assigned to the wrong cluster. For the first stage hierarchical clustering, major clusters were determined for a range of distance cutoff from 0.3 to 0.9 with an increment of 0.05. Then, the mean silhouette coefficient was determined for each distance cut off. The optimal distance cutoff was selected as that resulting in the highest mean silhouette score. For the second stage hierarchical clustering, the distance cutoff values varied between 0.02 and 0.6 with an increment of 0.001.

Select elemental ratios were determined on a particle-by-particle basis for all particles containing the two elements, and the elemental ratio distribution was determined. Particle sizes were calculated assuming the measured mass of each element is derived from a single pure particle. The particle sizes are used for comparisons among samples and not necessarily to infer an accurate size measurement of a given metal(loid) particles. The number concentration (NM g^{-1}) of the total, smNMs, mmNMs, and cluster members were determined according to SP-ICP-MS theory.[34] The INM particle sizes were determined assuming spherical shape and pure metal(loid) oxide phases (**Table S3**).

3. Results and Discussion

3.1. Bulk elemental composition

Carbon content vary between 2 and 26% of the ash mass and followed the order carbon in structural ash (2.0 to 5.1%) < carbon in vegetation and atmospheric deposition ash (6.2 to 10.7%)< carbon in vehicle ash (12.1 to 26.0%)[18]. Ten elements, including Al, Fe, Zn, Ti, Mn, Ba, Pb, Cu, Cr, and Sr, account for > 98% of the total measured elemental concentrations in each sample, with the exception of sample A5, in which these elements account for 91% of the total measured elemental concentrations, with Co, Ni, Sn, and Cd accounting for another 8% of the total measured elemental concentrations (**Figure 1**). All other measured elements account for < 0.4% in all ashes except in sample A5, in which they account for 1.6% of the total measured elemental concentrations.

The bulk elemental concentrations in the nine ashes show stark differences in their elemental composition.[18] The vegetation and atmospheric deposition ashes display similar elemental composition, with high Al and Fe concentrations, along with lower concentrations of Ti, Mn, Sr, and Ba (**Figure 1a**). The similar composition of the vegetation and atmospheric deposition ashes is because the atmospheric deposition ash was dominantly derived from the combustion of biomass. The elemental compositions of structural ashes are dominated by Al, Ti, Fe, and Zn, and to a lesser extent by Cr, Co, Cu, Ba, and Pb (**Figure 1b**). The elemental compositions of vehicle ashes are dominated by Al, Ti, Mn, Fe, Cu, Zn, and Pb, and to a lesser extent by Ba (**Figure 1c**). The ratio of metal concentration in structural and vehicle ash compared to vegetation and atmospheric deposition ash demonstrates that most metals are higher in structural and vehicle ash compared to vegetation ash (**Figure 1d**), in particular Cu, Zn, As, Mo, and Pb. In addition to the differences in the elemental compositions among the different groups of ashes, the bulk elemental ratios of Ti/Nb (*e.g.,* 480 to 13,990, **Figure 2a**) in all ashes are higher than the average crustal value (*e.g.,* 320)[38] and decrease in following the order: structural > vehicle > vegetation. Additionally, the elemental ratios of Cr/As in ashes also decrease according to the order: structural > vehicle > vegetation (**Figure 2b**). The elemental ratios of Sn/Fe (**Figure 2c**), Sb/Fe (**Figure 2d**), and Pb/Fe (**Figure 2e**) are higher in structural and vehicle ashes than those in vegetation ashes (Sb was below detection limit in vegetation ashes) and are higher than the average crustal values in all ashes, consistent with the anthropogenic nature of Sn, Sb, and Pb. These findings demonstrate that WUI fire ashes contain anthropogenic Ti, Cr, Sn, Sb, and Pb-bearing NMs. The differences in the elemental compositions and ratios in the different ashes are ascribed to the differences in the elemental compositions of the fuels (***see SI section for more details***).

3.2. Particle number concentration

Similar to the bulk elemental composition, few types of NMs (*e.g.,* Fe, Mn, Ti, Zn, Pb, Al, Cr, Ba, and Cu) account for > 95% of the total number of detected NMs, assuming each event occurred as an individual NM (**Figure 3a**), with the exception of A5, in which these types of NMs account for 89% of

the detected NMs with Ce, Co, La, Nb, Nd, Sn, and Zr accounting for another 10% of the total detected NMs. All other NM types account for < 4% in all ashes except in A5 in which they account for 11% of the total detected NMs. Rare earth elements other than La and Ce, as well as Hf, Ta, Th, W, and U were rarely detected in any of the ashes as single particles and thus were removed from data analysis and discussion. Ce and La NMs occurred in substantial numbers in A5 only. The absence/low frequency of REEs in the fire ashes (*e.g.,* relative abundance REE INMs compared to the total number of INMs <0.012 for La, <0.029 for Ce, <0.007 for Pr, and <0.007 for Nd) indicates the limited contribution of natural nanomaterial from soil to the WUI fire ashes because REEs occur at high frequency (*e.g.,* relative abundance of REE INMs compared to the total number of INMs = 0.47 to 2.14 for La, 1.0 to 4.0 for Ce, 0.09 to 0.58 for Pr, and 0.21 to 1.0 for Nd) in natural nanomaterials from soils.[32] Nonetheless, the most abundant INMs were different among the different ashes, suggesting substantial differences in the INM make up in the nine ashes, in good agreement with the bulk metal(loid) concentrations. The vegetation and atmospheric deposition ashes are dominated by Fe and Mn NMs (**Figure 3a**), which account for 80 to 90% of all detected NMs. The relatively low abundance of Al NMs is likely attributed to the large sizes of Al NMs and the higher size detection limit of Al NMs by SP-ICP-TOF-MS (*e.g.,* 250 nm assuming Al_2O_3) compared to other elements. Structural ashes were dominated by Fe, Ti, Zn, Mn, Cr, Ba, Al, and Pb, which together account for 87 to 95% of all detected NMs. Vehicle ashes were dominated by Zn, Fe, Ti, Mn, Pb, and Al, which together account for 93 to 97% of all detected NMs.

3.3. Single particle elemental composition

The majority of the detected INMs occurred as mmNMs with a few exceptions (**Figures S2b and c**). Among the INMs with high number concentrations, 93% and 60% of Fe in vegetation ashes (A1 and A2, respectively), 61% of Ti in A7, 53% of Mn in A9, and 57% of Zn in A8 occurred as smNMs. These differences in the relative abundance of smNMs *vs.* mmNMs can be ascribed to the source of the particles in the different ashes or because NMs may occur in the form of heteroaggregates. Note that mmNMs were rarely detected in the blanks, indicating that all mmNMs are true particles.

The automated two-stage hierarchical clustering generated an overall 29 clusters across all ash samples (**Figures 3b**). The elemental makes up and the abundance of mmNM clusters were different among the different in the nine ashes. Whereas some clusters were identified in all ashes, others were identified only in structural and vehicle ashes (**Figure 3b**). The majority of mmNMs (86 to 95%) in vegetation and atmospheric deposition ashes occur in the Fe-rich mmNM clusters (FeMnZn or FeMn). In contrast, structural and vehicle ashes contain mmNMs with a more diverse composition. The majority of mmNMs (86 to 97%) in structural ashes occur in the FeMnZn, TiFeZn, and AlFeZn clusters, which account for 10 to 77%, 19 to 62%, and 1 to 57% of all mmNMs, respectively. The majority of mmNMs (87 to 99%) in vehicle ashes occur in the FeMnZn, TiFeZn, AlFeZn, ZnFePb, and FeMnZn clusters, which account for 4 to 19%, 4 to 39%, 6 to 35%, 10 to 54%, and 0 to 46%, of all mmNMs, respectively. Other clusters such as CuFePb, CoAlCr, PbSbCe, CuPbCr, SnTiFe, PbSnBa, SbPb, and SbTi contain few members and occur only in structural and vehicle ashes. The elemental combinations within these clusters are indicative of anthropogenic sources of INMs.

The elemental compositions of the mmNMs are presented in **Figures 3c, S3, and S4**. Typically, the composition of each cluster is dominated by one metal(loid) and contains minor or trace concentration of other metal(loid)s. Some clusters, such as Fe (**Figure S3a and b**), Ti (**Figure S4c and b**), Al (**Figure S3e**), Mn (**Figure S3f and g**), Zr (**Figure S3h and i**), and Ba (**Figure S3j-l**) although they contain mmNMs with similar elemental combinations as natural mmNMs,[39, 40] they also contain other elements such as Pb, Cr, Zn, Ni, and Cu, which indicate heteroaggregation of Fe, Ti, Al, Mn with other NMs. Additionally, the elemental concentrations of the minor elements in these clusters are different than those present in natural mmNMs.[32] Other clusters, such as CeLaNd (**Figure S3m**), FeMn (**Figure S3n**), and NdLa (**Figure S3o**), contain mainly naturally occurring elements similar to mmNMs identified in uncontaminated natural soils.[32] Other clusters are rich with anthropogenic metal(loid)s such as Cu (**Figure S4a-c**), Cr (**Figure S4d**), Pb (**Figure S4e-g and j**), Sn (**Figure S4g-i**), Sb (**Figure S4j and k**), Zn (**Figure S4l**), Ni (**Figure S4m**), and Co (**Figure S4n**). Because some NMs occur as heteroaggregates of mmNMs (as discussed below), some mmNMs could represent a small mass fraction within mmNM

clusters and thus could be overlooked. Thus, the elemental ratios between commonly associated elements in mmNMs clusters were calculated for all mmNMs containing the two elements with the aim to identify mmNM particle types.

Cr and Cu-bearing INMs. Chromium and copper occurred as major elements in four clusters (**Figure S3a-d**). Based on the elemental composition of these clusters, Cr and Cu can be attributed to Cr and Cu alloys and/or chromated copper arsenate.[41-46] Chromium and Cu bearing mmNMs occur in association mainly in structural ashes (**Figure 4a**). The molar ratios of Cr/Cu in all Cr and Cu-bearing mmNMs range from 0.01 to 614 in A4 and are predominantly < 1.0, whereas those in A5 and A6 are predominantly > 1.0 (**Figure 4b**). These ratios indicate that the Cr and Cu-bearing mmNMs could be attributed to $CuCrO_2$, $CuCr_2O_4$ as well as aggregates of these phases with pure Cr-oxides such as CrO_3, CrO_2, Cr_2O_3 that form during the combustion of CCA-treated wood.[19] The relative lack of detection of As is likely due to the volatilization of As during the combustion process.[47, 48]

Copper and Pb, Cu and Sn, and Cu and Ni bearing mmNMs occur in association mainly in structural and vehicle ashes with highest number concentrations in the structural ash with a lower particle number concentration of Cu and Ni bearing mmNMs in the vegetation ash and CuPb and CuSn bearing mmNMs in the structural ashes (**Figure 4c**). The elemental ratios of Cu/Sn (**Figure 4c**) and Cu/Pb (**Figure 4d**) suggest the occurrence of Cu alloys such as 85-95%Cu5-15%Sn and CuPb alloys such as 70%Cu5%Sn25%Pb (Cu/Pb = 2.8), 88%Cu6%Sn1.5%Pb (Cu/Pb = 58.7), as well as other CuPb-bearing alloys with other elemental percentages.[49] The elemental ratio of Cu/Ni is < 2 in the vegetation ash (A1), but extends to 622 in the structural ash (A4, **Figure 4e**) indicating that those CuNi particles could have originated from CuNi alloys.[49]

Pb, Sn, and Sb-bearing INMs (alloys). Pb, Sb, and Sn bearing mmNMs occur mainly in structural ashes, less frequently in vehicle ashes, and were not detected in vegetation and atmospheric deposition ashes. Lead, Sb, and Sn occurred as major elements in seven mmNM clusters, including PbSbCe, PbSnBa, SnTiFe, SnSbFe, and SbPb clusters (**Figure S4f-j**) and in other clusters as minor elements (**Figure S3**). SbPb, SnPb, and SnSb bearing mmNMs occur primarily in structural ashes, at much lower

concentrations in vehicle ashes, and were not detected in vegetation and atmospheric deposition ashes (**Figure 5a**). The elemental ratios of Sb/Pb, Sn/Pb, and Sn/Sb in all mmNMs bearing these elemental combinations cover a broad range from 0.2 to >4.0 (**Figure 5b-d**). The Sb/Pb ratio is higher than the average crustal value of 0.024 and coincides with a series of SbPb mmNMs with the formula of Sb_yPb (y=1 to 5, **Figure 5b**).[50-52] The elemental ratios of Sn/Pb are greater than the average crustal value (0.12, **Figure 5c**) and cover those of pigments such as Pb_2SnO_4 (Sn/Pb = 0.29) and $SnPbO_4$ (Pb/Sn = 0.57), or SnPb alloys such as $PbSn_3$ (Sn/Pb = 1.71) and $PbSn_5$ (Sn/Pb = 2.86).[53] The elemental ratios of Sn/Sb are < the average crustal value (5.3, **Figure 5d**) and coincide with particles with molecular formula of $SnSb_3$, $SnSb_2$, SnSb, Sn_3Sb, likely semiconducting alloys with a formula Sn_xSb_y (x=2 to 4 and y = 3 to 5).[54] Sn, Sb, and Pb and a wide range of combinations of these elements are widely used as soldering alloys. Thus, SbPb, SnPb, and SnSb mmNMs could originate from soldering alloys,[49, 55] which are widely used in structures and vehicles.[56, 57] Furthermore, other Sn, Sb, Pb alloy combinations are also possible, including 92.5%Ti5%Al2.5%Sn (**Figure 5e**), 85-95%Cu5-15%Sn (**Figure 4d**).[49, 58] Lead is widely used in automotive, telecommunication, and backup power systems as lead-acid batteries due to its ability to store and deliver DC electrical energy reliably. Lead is also commonly used in electronics for joining components to circuit boards. Other major uses include ammunition, paints, cable sheathing, and sheet lead. Lead is heavily regulated in the plumping, paint, and gasoline industries. Lead-bearing solders, on the other hand, have been used extensively in the electronic industry since the early 1950s with less regulation.

Co and Al-bearing INMs. Co and Al-bearing INMs occurred in one cluster, mainly in structural ash (A5 and A6, **Figure S4n**). The elemental ratio of Co/Al is < 0.01 in the vegetation ash A1, but varied between 0.01 and 3 in most particles detected the structural ashes (82-96% of CoAl mmNMs) with the majority of particles, which can be attributed to CoAl alloys such as 50%Co50%Al (Co/Al = 1) and 67%Co33%Al (Co/Al = 2, **Figure S5**).[18]

Ti and Fe-bearing INMs. The majority (*e.g.,* 71 to 96%) of Ti and Fe bearing mmNMs in vegetation and atmospheric deposition ashes are characterized by Ti/Fe < 1.0 and are thus typical of those found in

natural NMs (**Figure S6a**).[32] In contrast, a smaller fraction (*e.g.,* 23-64%) of Ti and Fe-bearing mmNMs in the structural and vehicle ashes are characterized by Ti/Fe < 1.0 (**Figures S6b and c**). Furthermore, structural and vehicle ashes contain a substantial fraction (27 to 69%) of mmNMs with Ti/Fe > 2.0, with A6 and A7 having the highest fraction of mmNMs with Ti/Fe >2.0, accounting for 61 and 69% of all Fe- and Ti-bearing INMs. These observations indicate anthropogenic sources of Ti-bearing NMs in structural and vehicle ashes.

Al and Fe bearing mmNMs. The elemental ratios of Al/Fe display higher values in structural and vehicle ashes compared to vegetation ashes (**Figure S6d-f**). The majority (86 to 89%) of Al Fe bearing INMs in vegetation ashes are characterized by Al/Fe between 0 and 2. The majority (86%) of Al and Fe bearing INMs in the atmospheric deposition and A4 ashes are characterized by Al/Fe between 0.05 and 10. In contrast the majority (51 to 87%) of Al and Fe bearing mmNMs in structural and vehicle ashes are characterized by Al/Fe > 10. Aluminum and Fe-bearing INMs in vegetation ashes might be ascribed to contamination from soil mmNMs, the uptake of Al and Fe bearing INMs by vegetations, or the similar elemental ratios of Al/Fe in vegetations to natural mmNMs (Al and Fe concentrations in plants are 106 (25 to 355) mg kg^{-1} Al and 75 (37 to 443) mg kg^{-1} Fe, respectively).[59] In contrast, the high elemental ratios of Al/Fe in structural and vehicle ashes are ascribed to the use of the pure form of these elements in structural materials and vehicle components.

Cr and Fe-bearing INMs. The elemental ratios of Cr/Fe display higher values in structural and vehicle ashes compared to vegetation ashes (**Figure S6g-i**). Most likely, these differences in the elemental ratios are due to the heteroaggregation of Cr and Fe-bearing INMs in structural and vehicle ashes. The Cr/Fe ratios in vegetation ashes (<0.04 in A1 which has a significant number of Cr and Fe-bearing INMs) are close to those in the bulk vegetation (75 (37 to 443) mg kg^{-1} Fe, <0.2 mg kg^{-1} Cr[59]).

Zn, Fe, and Ti-bearing mmNMs. Zn and Fe-bearing mmNMs occurred in higher concentrations in structural and vehicle ashes than in vegetation ashes (**Figure 1**). The elemental ratios of Zn/Fe display higher values in vehicle ash than in structural ash than in vegetation and atmospheric deposition ash (**Figure S6j-l**). Additionally, given the common association between Ti and Zn in mmNMs, we plotted

the elemental ratios of Zn/Ti (**Figure S6m-o**). The elemental ratios of Zn/Ti in mmNMs decrease in ashes as follows: vehicle > structural > vegetation (**Figure S6j-l**). These observations further confirm the anthropogenic origin of Zn in the structural and vehicle ashes.

The high elemental ratios of Ti/Fe, Al/Fe, Cr/Fe and Zn/Fe in mmNMs determined by SP-ICP-TOF-MS are consistent with those determined by TEM-EDS (**Figure S7 and Table S4**) and are attributed to the occurrence of Ti, Al, Cr, and Zn as pure phases as demonstrated by TEM-EDS analysis (TEM images and EDS maps were presented in our previous study)[18]. The elemental composition of INMs in vegetation and atmospheric deposition ash is dominated by C,O,Ca, and Mg-bearing materials with small concentrations of other elements and absence of Cr, Cu, Co, and Pb (**Figure S7 and Table S4**). In contrast, INMs in structural and vehicle ash contained higher concentrations of Si, Al, Ti, Fe, Mn, and Zn. Cr and Pb were detected in structural ashes only. The types and composition of INMs detected by TEM are generally in good agreement with those detected by SP-ICP-TOF-MS. It is worth noting that the lack detection of a given type of nanomaterials (*e.g.,* Pb in vehicle ash) by TEM could be attributed to its low frequency in the WUI ash samples rather than to its absence.

3.4. Particle size

Substantial fractions of the detected particles by SP-ICP-TOF-MS were in the nanosize range (< 100 nm); 6 to 59% for Ti, 33 to 80% for Fe, 27 to 89% for Zn, 44 to 100% for Cr, 76 to 98% for Mn, 91 to 100% for Ba, 89 to 100% for Pb, 67 to 100% for Cu, 80 to 100% for Sn, 91 to 100% for Sb, (**Table 1 and Figure S8**), suggesting the efficient extraction of primary or small heteroaggregates of INMs from the fire ash. The median particle size of some INMs such as Al, Mn, Cu, Ba, Sb, and Pb-bearing INMs—assuming pure Al_2O_3, MnO_2, CuO, BaO, Sb_2O_3, and PbO phases— did not display substantial differences among the three types of ashes (**Table 1 and Figure S8**). In contrast, the median particle size of other elements such as Ti, Fe, Zn, Cr-bearing INMs—assuming pure TiO_2, Fe_2O_3, ZnO, and Cr_2O_3 phases— in structural ashes are larger than those in vehicle and vegetation ashes (**Table 1**). The differences in the median sizes of Ti, Fe, Zn, Cr among the different ashes can be ascribed to differences in the source of INMs in the different ashes. For instance, INMs in vegetation ashes most likely originate from the

metal(loid)s or natural nanomaterials taken up by plants, which may favor the formation/uptake of small NMs.[60] In contrast INMs in structural most likely originate from the breakdown of bulk metal(loid)-bearing objects (*e.g.,* pipes, electrical wires, appliances, *etc.*), or the use of engineered particles (*e.g.,* pigments and NMs) in structural materials such as paint and coatings, along with metal(loid)s stored in or added to wood.[61-64] For instance, Ti, Fe, and Zn oxides are widely used as pigments and fillers in paints and coatings. Chromium is a component of a widely used wood preservative —chromated copper arsenate (CCA, CrO_3, CuO, and As_2O_5) — which was used since the 1940s and phased out in the early 2000s in the U.S.[65] but remains in existing structures.[41-46] Metal(loid) alloys such as SnSb, SnPb, and SbPb are widely used in structures and vehicles.[49, 58, 66].

4. Conclusions

To the best of our knowledge, this study is the first of its kind to characterize the abundance and elemental makeup of inorganic, metal(loid) INMs formed as a result of the combustion of different types of fuels in WUI fires using SP-ICP-TOF-MS. Structural and vehicle fire ashes contain higher concentrations of metal(loid) INMs, in particular Fe, Ti, Zn, Mn, Cr, Cu, Sn, Sb, and Pb than those in vegetation ashes and atmospheric deposition ashes. Iron- and Mn-bearing INMs were the most abundant INMs in vegetation and atmospheric deposition ashes accounting for >80% of the detected INMs by SP-ICP-TOF-MS. In contrast, Fe- and Mn-bearing INMs accounted for <50% of the detected INMs by SP-ICP-TOF-MS in structural and vehicle ashes. Aluminum-, Ba-, Cr-, Cu-, Ti-, Pb-, and Zn-bearing INMs were more preponderant in structural and vehicle ashes (accounting for 45 to 75% of all INMs) than in vegetation and atmospheric deposition ashes (accounting for 7 to 13% of all INMs). The sizes of INMs varied between a few tens to a few hundreds of nanometers with larger Ba, Cr, Fe, Ti, Pb, and Zn-bearing INMs in structural and vehicles ashes than in vegetation ashes. Several mmNMs were also identified in the WUI fire ash, including chromated copper arsenate related NMs (*e.g.,* $CuCrO_2$, $CuCr_2O_4$); CuSn and CuPb alloys; SnPb, SbPb, and SnSb alloys; and CoAl alloys.

The identified metal(loid) INMs in fire ashes can be of social and environmental concern, impacting public health and safety, infrastructure, biodiversity, and contributing to land[18, 27, 28], water[29, 67], and air pollution,[68, 69] with potential impacts for living organisms within these environmental compartments.[4, 70] These INMs are likely to present public health risks to people (*e.g.,* fire recovery workers, residents) and communities through direct and indirect ingestion, inhalation, and absorption. People are likely to be exposed INMs present in ashes through disturbance and resuspension of the ashes (*e.g.,* from walking, cleaning, wind), which may be inhaled.[26] Health effects of ash exposure range from acute symptoms, such as coughing, sneezing, and throat and eye irritation, to chronic disease and increased cancer risk. The detected INMs might contribute to such effects. The environmental and human health implications of fire ashes, iron oxides, and chromated copper arsenate by-products have been discussed in our previous studies [18-20, 71], and those of other types of INMs such as Zn, Cu, and Cr oxides have been discussed in other studies in the literature [60]. The abundance of metal(loid) INMs in fire ashes and these potential environmental and human health effects demonstrate how additional research could be used to better understand the nature, concentrations, formation, transformation, reactivity, short- and long-term stability, fate, and effects of metal(loid) INMs during and after fires at the WUI. Topics for additional research could include: 1) experimental work on synthetic nanomaterials and various types of fuels under well controlled simulated WUI fire conditions to develop fundamental and mechanistic understanding into the formation and transformations of INM in WUI fires, 2) field investigations (similar to this study) to determine the real-environmental products resulting from to unknown transformations of INMs within the fire environment and after release into the environment, 3) mobilization and transport of WUI fire INMs to surface water following storm events, and 4) environmental and human health implications of the fire generated INMs.

Acknowledgments

This work was supported by a United States National Science Foundation grants (2101983 and 2345468) and the National Institute of Health grant (1R21ES037105-01) to Dr. Baalousha. This work was also supported by the Nanoscale Characterization and Fabrication Laboratory and the Virginia Tech National Center for Earth and Environmental Nanotechnology Infrastructure (NanoEarth), a member of the National Nanotechnology Coordinated Infrastructure (NNCI), supported by NSF (ECCS 1542100 and ECCS 2025151**).** Support was also provided by the U.S. Geological Survey through the Environmental Health Program of the Ecosystems Mission Area. Any use of trade, firm, or product names is for descriptive purposes only and does not imply endorsement by the U.S. Government.

Competing interest statement

The authors declare no competing interest.

Author Contributions

Mr. Mahbub Alam performed all experimental work, data analysis, and wrote the first draft. Dr. Mohammed Baalousha conceived the overall idea of the research, coordinated the collaboration among the research team, and supervised Mr. Mahbub Alam in performing experimental work and data analysis. Dr. Charles N. Alpers performed field sampling and provided background information on the sampling sites and the collected samples. Dr. Sheryl A. Singerling performed transmission electron microscopy analysis and the associated data analysis. All authors contributed to the manuscript writing and editing.

1. Cunningham CX, Williamson GJ, Bowman DMJS. Increasing frequency and intensity of the most extreme wildfires on Earth. Nature Ecology & Evolution. 2024.
2. Zong X, Tian X. Bibliometric analysis of fires on wildland-urban interfaces. Natural Hazards Research. 2022;2(3):147-53.
3. Bladon KD, Emelko MB, Silins U, Stone M. Wildfire and the future of water supply. ACS Publications; 2014.
4. Brito DQ, Passos CJS, Muniz DH, Oliveira-Filho EC. Aquatic ecotoxicity of ashes from Brazilian savanna wildfires. Environmental Science and Pollution Research. 2017;24(24):19671-82.
5. Wibbenmeyer M, McDarris A. Wildfires in the United States 101: Context and Consequences. https://www.rff.org/publications/explainers/wildfires-in-the-united-states-101-context-and-consequences/. Accessed 29 March 2022. 2021.
6. Williams AP, Cook ER, Smerdon JE, Cook BI, Abatzoglou JT, Bolles K, et al. Large contribution from anthropogenic warming to an emerging North American megadrought. Science. 2020;368(6488):314-8.
7. Miller JD, Safford H, Crimmins M, Thode AE. Quantitative evidence for increasing forest fire severity in the Sierra Nevada and southern Cascade Mountains, California and Nevada, USA. Ecosystems. 2009;12(1):16-32.
8. Juang CS, Williams AP, Abatzoglou J, Balch J, Hurteau M, Moritz M. Rapid growth of large forest fires drives the exponential response of annual forest-fire area to aridity in the western United States. Geophysical Research Letters. 2022;49(5):e2021GL097131.
9. Hoover K, Hanson LA. Wildfire statistics. Congressional Research Service. 2021;2.
10. Chen H, Chow AT, Li X-W, Ni H-G, Dahlgren RA, Zeng H, et al. Wildfire burn intensity affects the quantity and speciation of polycyclic aromatic hydrocarbons in soils. ACS Earth and Space Chemistry. 2018;2(12):1262-70.
11. Scholze M, Knorr W, Arnell NW, Prentice IC. A climate-change risk analysis for world ecosystems. Proceedings of the National Academy of Sciences. 2006;103(35):13116-20.
12. Lyu H, He Y, Tang J, Hecker M, Liu Q, Jones PD, et al. Effect of pyrolysis temperature on potential toxicity of biochar if applied to the environment. Environmental Pollution. 2016;218:1-7.
13. Godlewska P, Ok YS, Oleszczuk P. THE DARK SIDE OF BLACK GOLD: Ecotoxicological aspects of biochar and biochar-amended soils. Journal of Hazardous Materials. 2021;403:123833.
14. Buss W, Mašek O, Graham M, Wüst D. Inherent organic compounds in biochar–Their content, composition and potential toxic effects. Journal of Environmental Management. 2015;156:150-7.
15. Burling IR, Yokelson RJ, Griffith DWT, Johnson TJ, Veres P, Roberts JM, et al. Laboratory measurements of trace gas emissions from biomass burning of fuel types from the southeastern and southwestern United States. Atmos Chem Phys. 2010;10(22):11115-30.
16. Wu J, Tou F, Yang Y, Liu C, Hower JC, Baalousha M, et al. Metal-Containing Nanoparticles in Low-Rank Coal-Derived Fly Ash from China: Characterization and Implications toward Human Lung Toxicity. Environmental Science & Technology. 2021;55(10):6644-54.
17. EuropeanCommission. Commission Recommendation of 10.6.2022 on the definition of nanomaterial. Brussels, 10.6.2022 C(2022) 3689 final. European Commission. https://ec.europa.eu/environment/chemicals/nanotech/pdf/C_2022_3689_1_EN_ACT_part1_v6.pdf. Accessed 11 Oct 2022. 2022.
18. Alshehri T, Wang J, Singerling SA, Gigault J, Webster JP, Matiasek SJ, et al. Wildland-urban interface fire ashes as a major source of incidental nanomaterials. Journal of Hazardous Materials. 2023;443:130311.
19. Alam M, Alshehri T, Wang J, Singerling SA, Alpers CN, Baalousha M. Identification and quantification of Cr, Cu, and As incidental nanomaterials derived from CCA-treated wood in wildland-urban interface fire ashes. Journal of Hazardous Materials. 2023;445:130608.

20. Baalousha M, Desmau M, Singerling S, Webster JP, Matiasek S, Stern MA, et al. Discovery and potential ramifications of reduced iron-bearing nanomaterials—magnetite, wüstite, and zero valent iron—in wildland-urban interface fire ashes. Environmental Science Nano. 2022;9(4136):4149.
21. García-Marco S, González-Prieto S. Short-and medium-term effects of fire and fire-fighting chemicals on soil micronutrient availability. Science of the total environment. 2008;407(1):297-303.
22. Chambers D, Attiwill P. The ash-bed effect in Eucalyptus regnans forest: chemical, physical and microbiological changes in soil after heating or partial sterilisation. Australian Journal of Botany. 1994;42(6):739-49.
23. Gómez-Rey MX, Couto-Vázquez A, García-Marco S, González-Prieto SJ. Impact of fire and post-fire management techniques on soil chemical properties. Geoderma. 2013;195-196:155-64.
24. Parra JG, Rivero VC, Lopez TI. Forms of Mn in soils affected by a forest fire. Science of the Total Environment. 1996;181(3):231-6.
25. Sanchez-Garcia C, Santín C, Neris J, Sigmund G, Otero XL, Manley J, et al. Chemical characteristics of wildfire ash across the globe and their environmental and socio-economic implications. Environment International. 2023;178:108065.
26. Alexakis DE. Suburban areas in flames: Dispersion of potentially toxic elements from burned vegetation and buildings. Estimation of the associated ecological and human health risk. Environmental Research. 2020;183:109153.
27. Villarruel CM, Figueroa LA, Ranville JF. Quantification of Bioaccessible and Environmentally Relevant Trace Metals in Structure Ash from a Wildland–Urban Interface Fire. Environmental Science & Technology. 2024;58(5):2502-13.
28. Jech S, Adamchak C, Stokes SC, Wiltse ME, Callen J, VanderRoest J, et al. Determination of Soil Contamination at the Wildland-Urban Interface after the 2021 Marshall Fire in Colorado, USA. Environmental Science & Technology. 2024;58(9):4326-33.
29. Magliozzi LJ, Matiasek SJ, Alpers CN, Korak JA, McKnight D, Foster AL, et al. Wildland–urban interface wildfire increases metal contributions to stormwater runoff in Paradise, California. Environmental Science: Processes & Impacts. 2024;26(4):667-85.
30. Plumlee GS, Martin DA, Hoefen T, Kokaly R, Hageman P, Eckberg A, et al. Preliminary analytical results for ash and burned soils from the October 2007 southern California wildfires. US Geological Survey Open-File Report. 2007;1407:13.
31. Burton CA, Hoefen TM, Plumlee GS, Baumberger KL, Backlin AR, Gallegos E, et al. Trace elements in stormflow, ash, and burned soil following the 2009 station fire in Southern California. PLoS One. 2016;11(5):e0153372.
32. Baalousha M, Wang J, Erfani M, Goharian E. Elemental fingerprints in natural nanomaterials determined using SP-ICP-TOF-MS and clustering analysis. Science of The Total Environment. 2021;792:148426.
33. Wang J, Nabi MDM, Erfani M, Goharian E, Baalousha M. Identification and quantification of anthropogenic nanomaterials in urban rain and runoff using single particle-inductively coupled plasma-time of flight-mass spectrometry. Environmental Science Nano. 2022;9:714-29.
34. Pace HE, Rogers NJ, Jarolimek C, Coleman VA, Higgins CP, Ranville JF. Determining transport efficiency for the purpose of counting and sizing nanoparticles via single particle inductively coupled plasma mass spectrometry. Analytical chemistry. 2011;83(24):9361-9.
35. Gundlach-Graham A, Hendriks L, Mehrabi K, Günther D. Monte Carlo Simulation of Low-Count Signals in Time-of-Flight Mass Spectrometry and Its Application to Single-Particle Detection. Analytical Chemistry. 2018;90(20):11847-55.
36. Mehrabi K, Kaegi R, Günther D, Gundlach-Graham A. Emerging investigator series: automated single-nanoparticle quantification and classification: a holistic study of particles into and out of wastewater treatment plants in Switzerland. Environmental Science: Nano. 2021;8:1211.

37. Rousseeuw PJ. Silhouettes: A graphical aid to the interpretation and validation of cluster analysis. Journal of Computational and Applied Mathematics. 1987;20:53-65.
38. Rudnick R, Gao S, Holland H, Turekian K. Composition of the continental crust. The crust. 2003;3:1-64.
39. Loosli F, Wang J, Rothenberg S, Bizimis M, Winkler C, Borovinskaya O, et al. Sewage spills are a major source of titanium dioxide engineered (nano)-particle release into the environment. Environmental Science Nano. 2019;6(3):763-77.
40. Gondikas A, von der Kammer F, Kaegi R, Borovinskaya O, Neubauer E, Navratilova J, et al. Where is the nano? Analytical approaches for the detection and quantification of TiO 2 engineered nanoparticles in surface waters. Environmental Science: Nano. 2018;5(2):313-26.
41. Chen AY-Y, Olsen T. Chromated copper arsenate–treated wood: a potential source of arsenic exposure and toxicity in dermatology. International Journal of Women's Dermatology. 2016;2(1):28-30.
42. de Medeiros Domingos D, Scussel R, Canever SB, Soares BQ, Angioletto E, Bernardin AM, et al. Toxicity of fly ash effluent from the combustion of (chromated copper arsenate)-treated wood. Cleaner Materials. 2022;3:100051.
43. Jambeck J, Weitz K, Solo-Gabriele H, Townsend T, Thorneloe S. CCA-Treated wood disposed in landfills and life-cycle trade-offs with waste-to-energy and MSW landfill disposal. Waste Management. 2007;27(8):S21-S8.
44. Helsen L, Van den Bulck E, Mullens S, Mullens J. Low-temperature pyrolysis of CCA-treated wood: thermogravimetric analysis. Journal of Analytical and Applied Pyrolysis. 1999;52(1):65-86.
45. Helsen L, Van den Bulck E. Review of disposal technologies for chromated copper arsenate (CCA) treated wood waste, with detailed analyses of thermochemical conversion processes. Environmental pollution. 2005;134(2):301-14.
46. Solo-Gabriele HM, Townsend TG, Messick B, Calitu V. Characteristics of chromated copper arsenate-treated wood ash. Journal of Hazardous Materials. 2002;89(2):213-32.
47. Wang C, Liu H, Zhang Y, Zou C, Anthony EJ. Review of arsenic behavior during coal combustion: Volatilization, transformation, emission and removal technologies. Progress in Energy and Combustion Science. 2018;68:1-28.
48. Clifford DA, Chen S-S, Reznik C. Volatilizing toxic metals from soil. Waste Management. 1993;13(5):467-79.
49. Habashi F. Alloys: preparation, properties, applications: John Wiley & Sons; 2008.
50. Li X, Qu J, Zhao Z, Zhao Y, Xie H, Yin H. Electrochemical desulfurization of galena-stibnite in molten salts to prepare liquid Sb–Pb alloy for liquid metal battery. Journal of Cleaner Production. 2021;312:127779.
51. Liu J-J, Lee M-W. Lead Antimony Sulfide Semiconductor-Sensitized Solar Cells. Electrochimica Acta. 2014;119:59-63.
52. Bagshaw NE. Lead alloys: past, present and future. Journal of Power Sources. 1995;53(1):25-30.
53. Hofmann W. Lead and lead alloys: Springer; 1970.
54. Kamal M, Abdel-Salam A, Pieri JC. Modification in tin-antimony alloys. Journal of Materials Science. 1984;19(12):3880-6.
55. Solder alloys. https://en.wikipedia.org/wiki/Solder_alloys#cite_note-53 [
56. Lipowsky H, Arpaci E. Copper in the automotive industry: John Wiley & Sons; 2008.
57. Amato F, Font O, Moreno N, Alastuey A, Querol X. Mineralogy and elemental composition of brake pads of common use in Spain. Macla. 2012;16:154-6.
58. Sharma CP. Engineering materials: properties and applications of metals and alloys: PHI Learning Pvt. Ltd.; 2003.

59. Reimann C, Koller F, Frengstad B, Kashulina G, Niskavaara H, Englmaier P. Comparison of the element composition in several plant species and their substrate from a 1 500 000-km2 area in Northern Europe. Science of the Total Environment. 2001;278(1-3):87-112.
60. Lead JR, Batley GE, Alvarez PJ, Croteau MN, Handy RD, McLaughlin MJ, et al. Nanomaterials in the environment: behavior, fate, bioavailability, and effects—an updated review. Environmental toxicology and chemistry. 2018;37(8):2029-63.
61. GII Global Information. Titanium Dioxide (TiO2) - A Global Market Overview. https://www.giiresearch.com/report/inde1404118-titanium-dioxide-tio2-global-market-overview.html?utm_source=chatgpt.com. 2024. Report No.: CP040.
62. Linak E, Inoguchi Y. Chemical Economics Handbook: Titanium Dioxide‖. Menlo Park, CA, SRI Consulting. 2005.
63. Ober JA. Mineral resource of the month: Iron oxide pigments. Earth Magazine. 2008.
64. United States Geological Survey. Mineral commodity summaries 2021, 200 p., https://doi.org/10.3133/mcs2021.; 2021.
65. United States Environmental Protection Agency. Chromated Arsenicals (CCA), https://www.epa.gov/ingredients-used-pesticide-products/chromated-arsenicals-cca2024 03/03/2024.
66. King M, Ramachandran V, Prengaman RD, DeVito SC, Breen J, Staff Ub. Lead and lead alloys. Kirk-Othmer Encyclopedia of Chemical Technology. 2000.
67. Bladon KD, Emelko MB, Silins U, Stone M. Wildfire and the Future of Water Supply. Environmental Science & Technology. 2014;48(16):8936-43.
68. Katie B, Stephen D L, Byron RR, Parker F D, Kristen M F, Amara H, et al. Beyond Particulate Matter Mass: Heightened Levels of Lead and Other Pollutants Associated with Destructive Fire Events in California. Environmental Science & Technology. 2022.
69. CARB. Camp Fire Air Quality Data Analysis. Sacramento, CA: California Air Resources Board; 2021 July 2021.
70. Paul MJ, LeDuc SD, Boaggio K, Herrick JD, Kaylor SD, Lassiter MG, et al. Effects of air pollutants from wildfires on downwind ecosystems: observations, knowledge gaps, and questions for assessing risk. Environmental science & technology. 2023;57(40):14787-96.
71. Alam M, Sitter JD, Vannucci AK, Webster JP, Matiasek SJ, Alpers CN, et al. Environmentally persistent free radicals and other paramagnetic species in wildland-urban interface fire ashes. Chemosphere. 2024;363:142950.

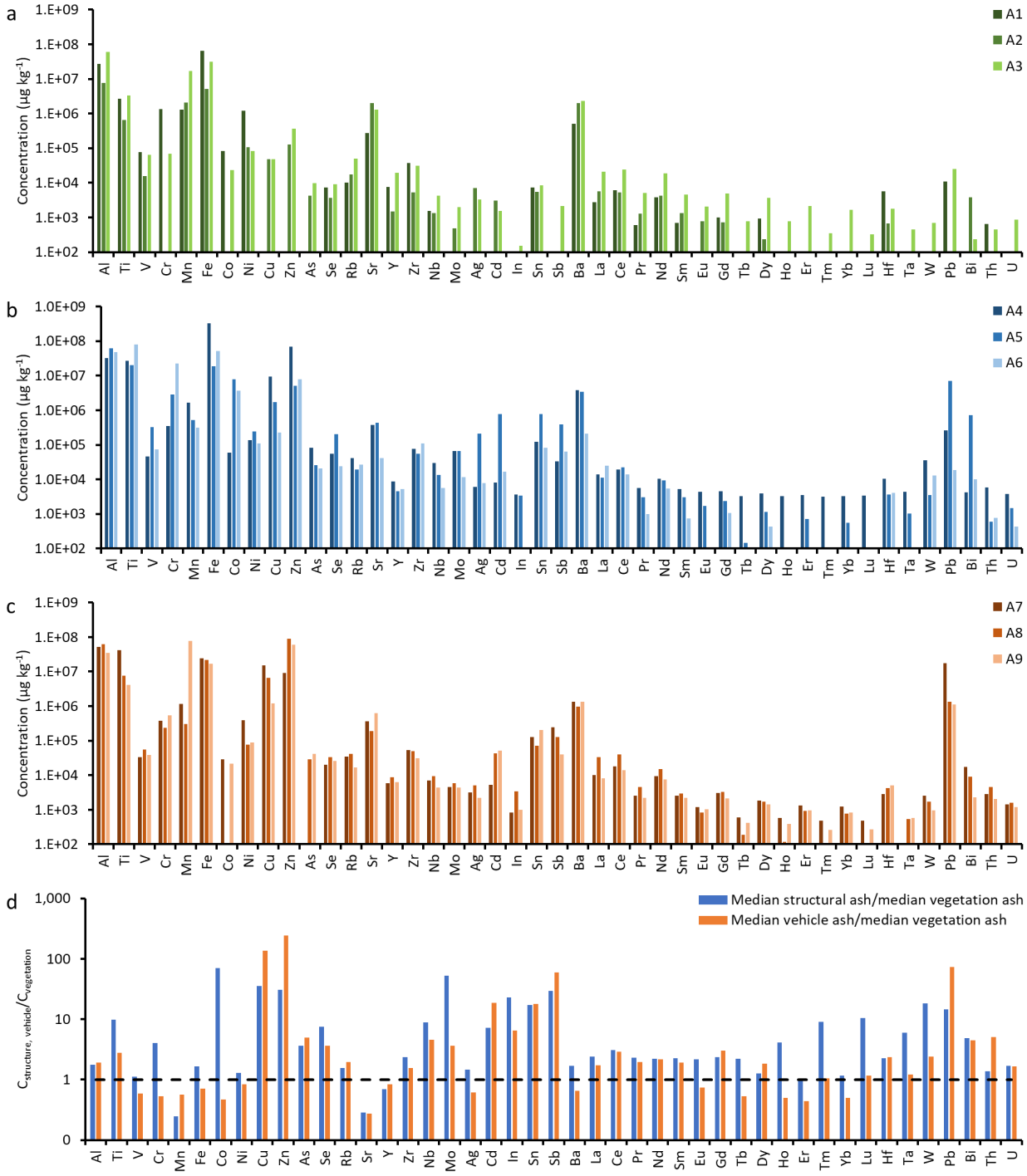

Figure 1. Bulk metal concentrations in the bulk ash samples: (a) vegetation and atmospheric deposition ashes, (b) structural ashes, (c) vehicle ashes, and relative concentration of metals in structural or vehicle ash compared to those in vegetation and atmospheric deposition ash.

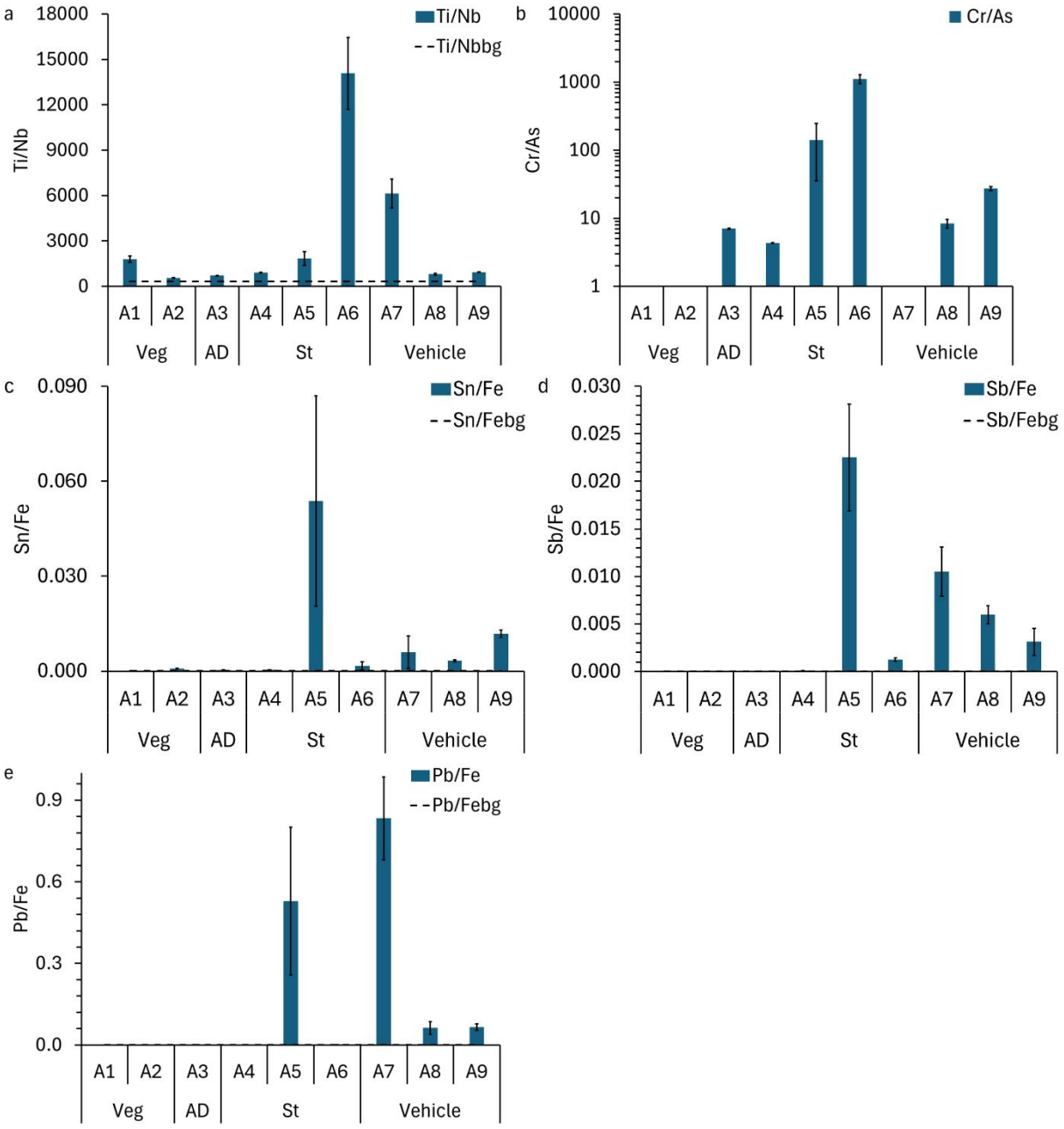

Figure 2. Bulk mass ratios of (a) Ti/Nb, (b) Cr/As, (c) Sn/Fe, and (d) Sb/Fe in the selected ash samples from different sources including vegetation (Veg), atmospheric deposition (AD), Structural (St), and Vehicle ashes. Ti/Nbbg, Sn/Febg, Sb/Febg and Pb/Febg refer to the average crustal elemental ratios and are 320, 0.00005, 0.00001, and 0.0004, respectively. The error bars represent the standard deviation of three replicates. The mean Ti/Nb ratios are different (ANOVA, $P < 0.05$) among all samples other than the pairs A1 *vs.* A5 and A4 *vs.* A9. The mean Cr/As ratios are different ($P < 0.05$) among all samples other than the pairs A5 *vs.* A9 and A3 *vs.* A8. The mean Sn/Fe ratios are different ($P < 0.05$) among all samples other than the pairs A5 *vs.* A7, A8, and A9; A6 *vs.* A1, A2, A3, A4, A7, A8; A7 *vs.* A1, A2, A3, A4, A8, and A9. The mean Sb/Fe ratios are different ($P < 0.05$) among all samples other than the pair A6 *vs.* A9. The mean Pb/Fe ratios are different ($P < 0.05$) among all samples other than the pairs A1 *vs.* A6; A3 *vs.* A4; A5 *vs.* A7; and A8 *vs.* A9.

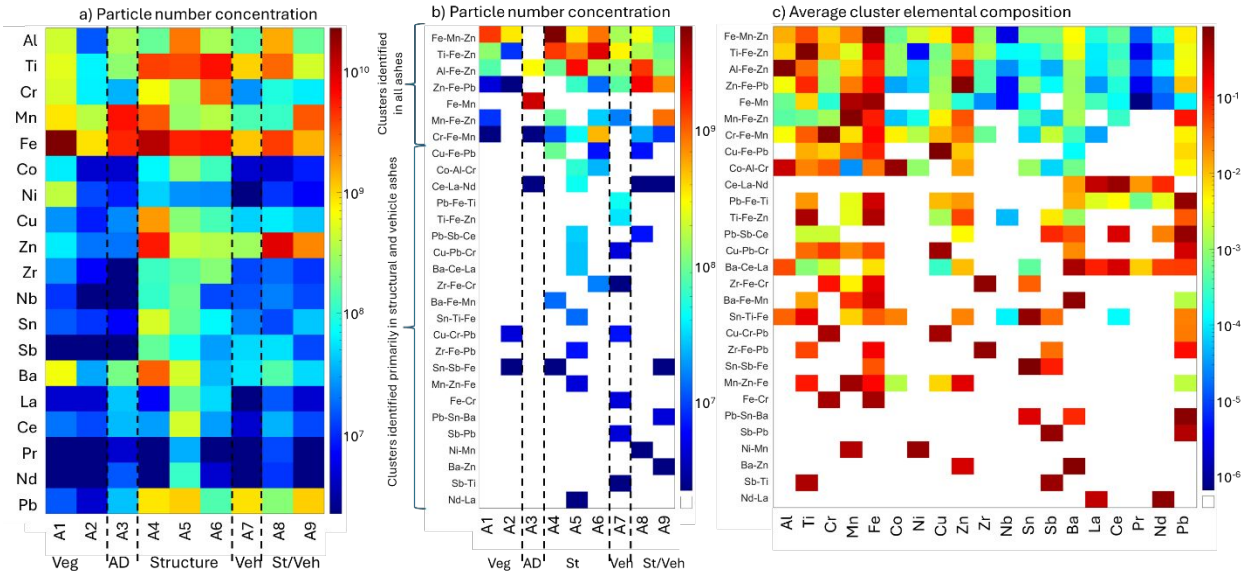

Figure 3. Particle number concentration (NM g^{-1}) of (a) individual elements in wildland-urban interface (WUI) fire ash from different sources including vegetation (A1, A2), atmospheric deposition (A3), structures (A4, A5, and A6), vehicle (A7) and mixed structures/vehicles (A8 and A9), (b) multi-metal nanomaterials (mmNMs) in mmNM clusters, and (c) average mmNM cluster composition. Veg: vegetation, AD: atmospheric deposition, St: structures, Veh: vehicles. The vertical dashed lines are used to guide the eye.

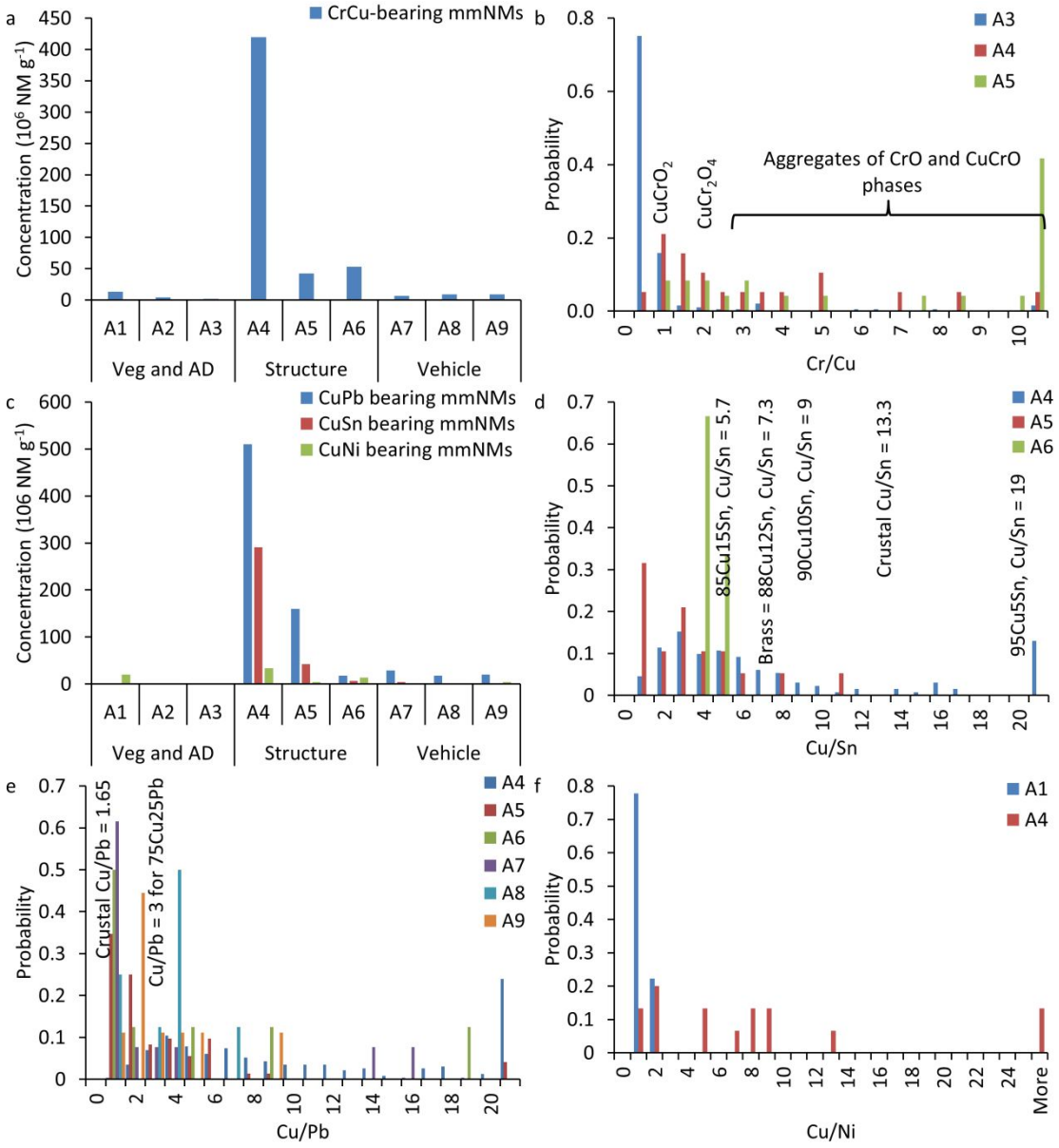

Figure 4. Number concentration of (a) Cr and Cu-bearing multi-metal nanomaterials (mmNMs) and (c) Cu and Pb, Cu and Sn, and Cu and Ni bearing mmNMs in wildland-urban interface (WUI) fire ashes collected from different sources including vegetation (A1, A2), atmospheric deposition (A3), structures (A4, A5, and A6), vehicle (A7) and mixed structures/vehicles (A8 and A9), (b) molar ratios of Cr/Cu in Cr and Cu-bearing mmNMs extracted from atmospheric deposition and structural ashes, (d) mass ratio of Cu/Sn (n = 3 to 131) in Cu and Sn-bearing mmNMs extracted from structural ashes, (e) mass ratio of Cu/Pb (n = 24 to 189) in Cu and Pb-bearing mmNMs extracted from structural and vehicle ashes, and (f) mass ratio of Cu/Ni (n = 9 to 15) in vegetation and structural ashes. Veg: vegetation, AD: atmospheric deposition, and n: number of detected particles by single particle-inductively coupled plasma-time of flight-mass spectrometer (SP-ICP-TOF-MS).

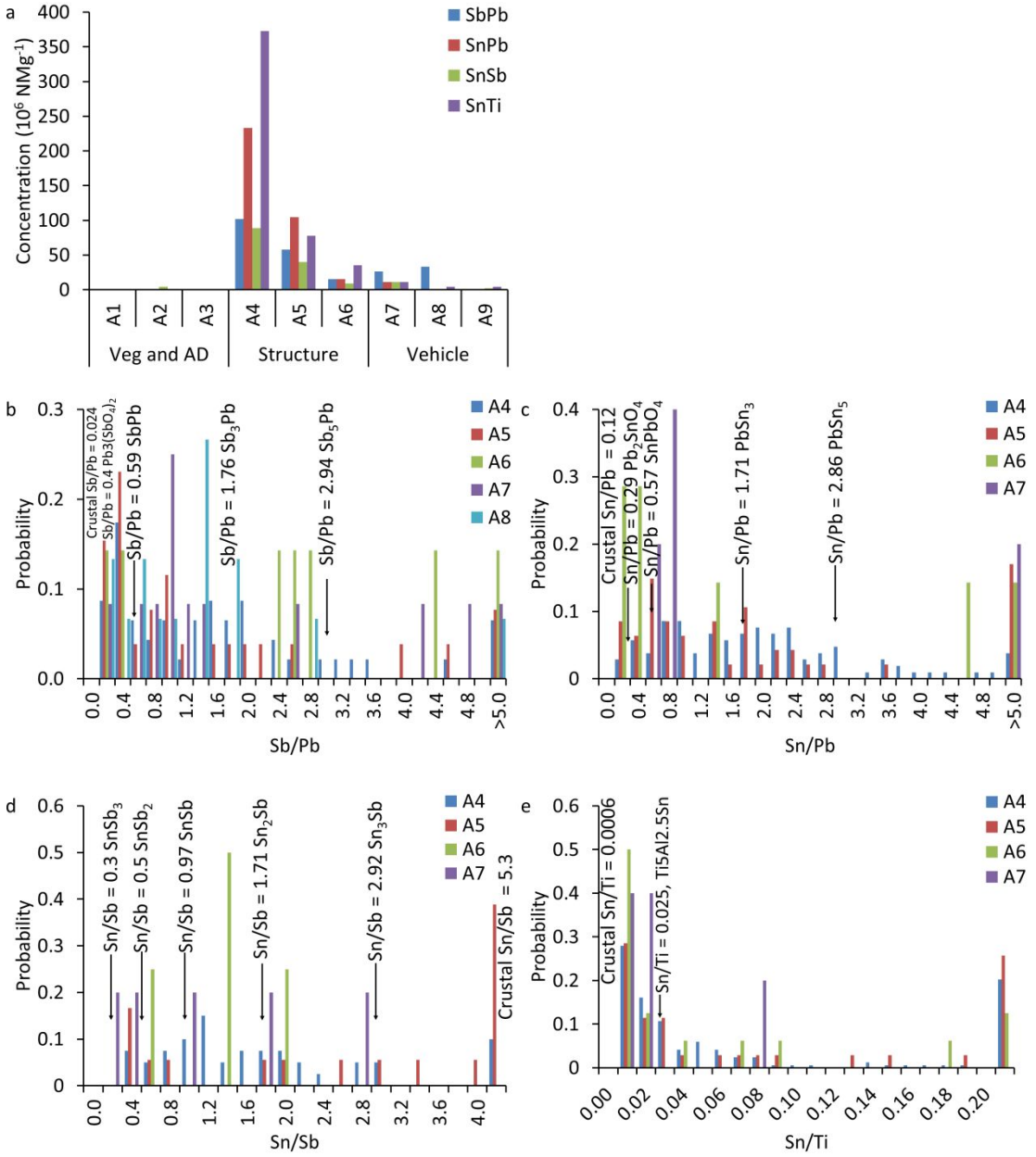

Figure 5. (a) Number concentration of SbPb, SnPb, SnSb, and SnTi-bearing multi-metal nanomaterials (mmNMs) in wildland-urban interface (WUI) fire ashes collected from different sources including vegetation (A1, A2), atmospheric deposition (A3), structures (A4, A5, and A6), vehicle (A7) and mixed structures/vehicles (A8 and A9). Elemental ratios together with suggested phases: (b) Sb/Pb ratios in SbPb-bearing multi-metal nanomaterials (mmNMs, n = 7 to 46), (c) Sn/Pb ratios in SnPb-bearing mmNMs (n = 5 to 105), (d) Sn/Sb in SnSb-bearing mmNMs (n = 4 to 40), and (e) Sn/Ti in SnTi-bearing mmNMs (n = 5 to 168). n: number of detected particles by single particle-inductively coupled plasma-time of flight-mass spectrometer (SP-ICP-TOF-MS).

Table 1. Descriptive statistical analysis of particle size distributions.

		Vegetation		Atmospheric	Structural			Vehicle	Structural/vehicle	
		A1	A2	A3	A4	A5	A6	A7	A8	A9
Ti	Median	94	135	96	200	111	269	204	94	121
	% < 100 nm	58	31	55	19	38	6	16	59	37
Fe	Median	94	80	90	132	86	131	79	78	76
	% < 100 nm	57	70	63	33	67	33	74	80	77
Zn	Median	87	95	87	139	92	97	91	104	107
	% < 100 nm	74	67	89	27	61	58	65	43	42
Cr	Median	66	68	64	66	98	110	67	79	72
	% < 100 nm	93	85	93	90	52	44	100	66	81
Al	Median	273	301	280	268	293	275	264	269	274
	% < 100 nm	0	0	0	0	0	0	0	0	0
Mn	Median	66	66	78	72	63	69	60	63	76
	% < 100 nm	90	86	76	82	87	80	89	98	79
Ba	Median	40	38	44	51	45	40	34	36	39
	% < 100 nm	100	100	99	91	96	94	96	99	96
Pb	Median	32	37	34	34	41	35	42	35	37
	% < 100 nm	100	100	89	100	96	98	95	98	100
Cu	Median	72	76	70	84	75	68	74	67	65
	% < 100 nm	100	75	82	67	86	92	86	89	84
Sn	Median	58	88	77	51	55	53	54	57	55
	% < 100 nm	86	80	100	100	87	97	100	100	89
Sb	Median	-	52	54	50	57	55	51	56	53
	% < 100 nm	-	100	100	97	89	100	91	92	100

Median is to median particle diameter.
% <100 nm is the % of particles with diameters smaller than 100 nm

Data availability statement

Data will be made available upon request.